Sunlight-driven selective oxidation of glycerol on formate oxidase mimicking AuPt/TiO$_2$

Xiaoyuan Liu [a,b], Yu Zou [b], Jiang Jiang [a,b,*]

[a] *Key Laboratory of Precision and Intelligent Chemistry, School of Nano-Tech and Nano-Bionics, University of Science and Technology of China, Hefei 230026, China*
[b] *i-Lab, CAS Key Laboratory of Nano-Bio Interface, Suzhou Institute of Nano-Tech and Nano-Bionics, Chinese Academy of Sciences, Suzhou 215123, China*

ARTICLE INFO

ABSTRACT

We report selective photocatalytic partial oxidation of glycerol on bimetallic formate oxidase mimicking AuPt/TiO$_2$, with a unique self-accelerating reaction kinetics discovered for the first time. Systematic investigation on the glycerol oxidation in the presence of externally added formic acid and various scavengers reveals a positive correlation between photocatalytic activity and solution H$_2$O$_2$ level. A reaction mechanism has been put forward, where the in situ generated formic acid consumes photogenerated holes, and enables on-site H$_2$O$_2$ production on AuPt/TiO$_2$, resulting in accelerated glycerol oxidation and improved C3 product selectivity. In pH 9 borate buffer solution, C3 products selectivity of 72% (60% for glyceric acid) has been achieved at 90% glycerol conversion under AM 1.5 G irradiation for 4 h, at ambient conditions. Our findings presented here may help guiding catalyst design for the photocatalytic biomass valorization in the future.

1. Introduction

Glycerol, one of the most important platform molecules, is generated in great surplus as a primary byproduct in the worldwide bio-diesel and soap industry [1]. Selective oxidation of the terminal, middle, or both hydroxyl groups in glycerol can produce a variety of valuable C3 products, including 1,3-dihydroxyacetone (DHA), glyceraldehyde (GLAD), glyceric acid (GLA), hydroxypyruvic acid (HPA), and tartronic acid (TA), which are of great importance in various industry such as cosmetics and pharmaceuticals sectors. [2–4]

Utilizing green and inexhaustible solar energy to valorize glycerol under ambient conditions can be a sustainable and energy-efficient way of converting glycerol to valuable chemicals [5–11]. For instance, noble metal nanoparticles (NPs) supported on TiO$_2$ semiconductor substrates have been constructed to drive aerobic photocatalytic glycerol oxidation reactions [12–16]. However, photoexcited e$^-$/h$^+$ pairs can generate a variety of reactive oxygen species (ROS) such as ·O$_2^-$ and ·OH in oxygenated water [17–20], which often leads to over-oxidized C2 and C1 products by breaking C-C bond, producing oxalic acid (OA), formic acid (FA), or even CO$_2$[21,22]. In our previous studies, we have shown that borate additives can not only coordinate and protect C3 intermediates from C-C bond breakage [23,24], but also regulate solution

ROS, enabling a balanced oxidative environment for selective glycerol oxidation on Au/TiO$_2$ photocatalysts [25]. However, the overall selectivity toward C3 products was still limited (~37% at 94% glycerol conversion), due to their inevitable complete mineralization. Further optimization of the solution oxidative power is therefore required to achieve more selective partial glycerol oxidation.

Apart from O$_2$, H$_2$O$_2$ is another environmental benign and mild oxidant for the oxidation of organic molecules [26–28]. For example, oxidation of alcohols to aldehydes has been realized with good selectivity by using H$_2$O$_2$[29]. Research endeavors have been devoted to use H$_2$O$_2$ for the direct oxidization of glycerol, on a variety of catalysts, such as metal complex or nanoparticles supported on SiO$_2$, carbon, and metal oxides [30–34], while the products distribution varied considerably among different catalysts. To circumvent the problems of storage and transport with the premade H$_2$O$_2$, Hutchings et al. reported oxidation of glycerol via in situ H$_2$O$_2$ synthesis from gaseous H$_2$ and O$_2$ on bimetallic Pd-Fe/TiO$_2$ under ambient temperatures, which however turned out to be non-selective towards any specific product.[35]

It is interesting to note that some noble metal/transition metal oxide catalysts are also known to be able to produce H$_2$O$_2$ under photo-excitations [36–39]. Furthermore, the addition of certain organic molecules, serving as the electron donors and proton sources, can enhance the

efficiency of photocatalytic H_2O_2 production. For instance, Shiraishi et al. reported the photocatalytic H_2O_2 production on bimetallic AuAg/TiO$_2$ in O_2 saturated ethanol/water mixed solution [40]. Tada et al. discovered that by adding 4% formic acid, H_2O_2 generation on Au/TiO$_2$ with bimodal size distribution can be greatly improved [41]. This made us ponder whether the inevitably formed FA during the photocatalytic glycerol oxidation could be used to assist the in situ H_2O_2 production, and to change the reaction kinetics and product distributions under ambient reaction conditions. Nanomaterial-based artificial enzymes or nanozymes have been enthusiastically pursued in the field of nanomedicine, as they display many intriguing enzymatic activity that mimics natural enzymes such as oxidase, peroxidase, catalase, and superoxide dismutase, without the need of constructing specific 3D structural domains for substrate recognition and binding [42]. The application of nanozyme in the photocatalysis can be potentially energy and cost efficient, as illustrated in Scheme 1.

Inspired by the findings that the noble metal Pd [43,44] and bimetallic AuPd [45], AuPt [46] could be used for on-site H_2O_2 production using FA and O_2 as feedstock, thus displaying a formic acid oxidase-mimicking activity, we describe herein selective photocatalytic glycerol oxidation on AuPt/TiO$_2$ under ambient conditions with a unique self-accelerating kinetics for the first time. By colorimetric and quasi-in-situ Raman spectroscopy analysis, the bimetallic alloy AuPt on TiO$_2$ has been shown to promote solution and surface peroxide species generation in the presence of formic acid under solar light irradiation, which is not the case for similarly prepared monometallic Au or Pt on TiO$_2$. Furthermore, by systematic investigation of glycerol oxidation activity in the presence of externally added formic acid, and the relationship of glycerol oxidation activity to the solution H_2O_2 levels using various scavengers, a tentative reaction mechanism is proposed to interpret the self-accelerating reaction kinetics and the selective glyceric acid production. The in situ produced formic acid not only consumes photogenerated holes, but also facilitates on-site H_2O_2 generation, thus speeding up the glycerol oxidation rate and improving C3 products selectivity.
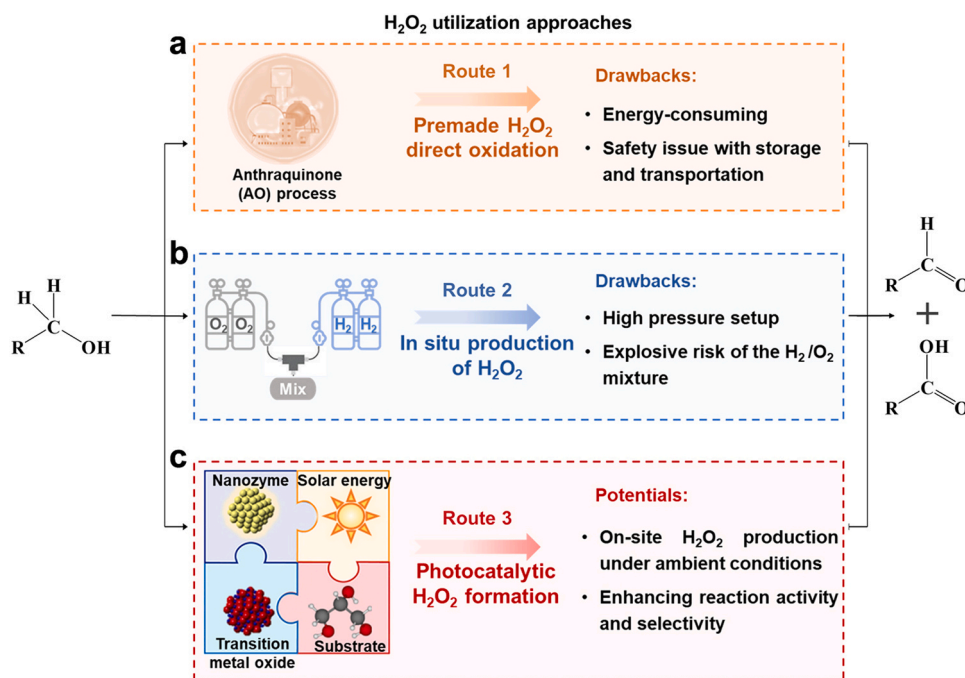
2. Experimental section

2.1. Chemicals

Aqueous HAuCl$_4$·3 H$_2$O solution (15.4 mM, Sinopharm) and H$_2$PtCl$_6$·6 H$_2$O solution (50 mM, UIV CHEM) were used as the metal precursors after proper dilutions with deionized water (Milli-Q grade). The TiO$_2$ support (Aeroxide® P25, 99.5%) was purchased from Sigma-Aldrich. Poly(vinyl alcohol) (PVA 1788, 87–89% alcoholysis), methylene blue (MB, 95%), nitroblue tetrazolium (NBT, 98%), 3,3′5,5′-tetramethylbenzidine dihydrochloride hydrate (TMB, 98%), DL-glyceric acid (C$_3$H$_6$O$_4$, 95%), hydroxypyruvic acid (C$_3$H$_4$O$_4$, 95%), tartronic acid (C$_3$H$_4$O$_5$, 98%), glycolic acid (C$_2$H$_4$O$_3$, 98%) and glyoxylic acid (C$_2$H$_2$O$_3$, 98%) were purchased from Aladdin Chemistry Co., Ltd. Sodium borohydride (NaBH$_4$, 96%), formic acid (HCOOH, 99.5%), sulfuric acid (H$_2$SO$_4$, 98%), sodium hydroxide (NaOH, 97%), sodium sulfate (Na$_2$SO$_4$, 99%), sodium tetraborate decahydrate (Na$_2$B$_4$O$_7$·10 H$_2$O, 99.5%), boric acid (H$_3$BO$_3$, 99.8%), cobalt (II) sulfate heptahydrate (CoSO$_4$·7 H$_2$O, 99.5%), potassium bicarbonate (KHCO$_3$, 99.5%), hydrogen peroxide aqueous solution (H$_2$O$_2$, 30%), silver nitrate (AgNO$_3$, 99.8%), triethanolamine (C$_6$H$_{15}$NO$_3$, 99.7%), isopropanol (C$_3$H$_8$O, 99.7%), glycerol (C$_3$H$_8$O$_3$, 99%), DL-glyceraldehyde (C$_3$H$_6$O$_3$, 90%), dihydroxyacetone (C$_3$H$_6$O$_3$, 99%), lactic acid (C$_3$H$_6$O$_3$, 97%) and oxalic acid (C$_2$H$_2$O$_4$, 99.5%) were purchased from Sinopharm Chemical Reagent Co., Ltd. Superoxide dismutase (SOD, 99%) was purchased from Beyotime Biotech. Inc.

2.2. Catalyst preparation

The noble metal supported photocatalysts were prepared based on the sol immobilization protocol reported in the previous literatures [47, 48]. The required amount of HAuCl$_4$ and H$_2$PtCl$_4$ solution were added into 70 mL deionized water under vigorous stirring to prepare AuPt colloids with an equal atomic ratio of Au and Pt. 1 wt% PVA aqueous solution was added to the uniformly dispersed mixture as a stabilizer to reach a PVA/metal mass ratio of 1.2. Then, freshly prepared 0.1 M NaBH$_4$ solution with ice water was added dropwise to the above solution until reaching a NaBH$_4$/metal molar ratio of 5, and a dark brown

Scheme 1. Comparison of catalytic alcohol oxidation by (a) premade H_2O_2, and in situ produced H_2O_2 by (b) H_2/O_2 gas mixture or (c) nanozyme catalysis.

solution formed instantaneously. After continuous stirring for half an hour, pre-dispersed TiO$_2$ suspension was blended in and immediately acidified with H$_2$SO$_4$ to pH 1 ∼ 2, which made it easier to interact with the metal nanoparticles. The immobilization procedure was carried out in the dark at room temperature for 2 h. Finally, the resulting gray precipitate was washed thoroughly with copious deionized water and ethanol before drying in a vacuum oven at 80 °C overnight. Mono-metallic Au or Pt on TiO$_2$ was prepared similarly.

2.3. Catalyst characterization

Morphologies of the monometallic and bimetallic catalysts were acquired using transmission electron microscopy (TEM), operated on HT7700 at 100 kV. The morphology and particle size distribution of AuPt/TiO$_2$ were acquired and analyzed via high-angle annular dark-field scanning transmission electron microscopy (HAADF-STEM) on the FEI Technai G2 F20 instrument at an acceleration voltage of 200 kV. The elemental mapping of Au and Pt was obtained via X-ray energy-dispersive spectrometer (EDS) by line-scan mode.

X-ray diffraction (XRD) patterns were recorded by a Bruker D8 diffractometer with Cu K α radiation (λ = 1.54 Å) measured at 40 kV and 40 mA. The scanning range of 20°-90° was selected, with a scanning speed of 10°/min. The baseline correction and phase matching were analyzed by JADE software.

X-ray photoelectron spectroscopy (XPS) was performed on a Thermo Scientific K-Alpha spectrometer. The fresh samples were analyzed using Al Kα radiation operating at 72 W (6 mA × 12 kV). Pass energy of 50 eV was used for high resolution spectra with the corresponding step size of 0.1 eV. The C 1s reference peak (284.8 eV) was used for the calibration of binding energies.

UV−vis−NIR diffuse-reflectance spectroscopy (UV−vis−NIR DRS) was conducted on a Shimadzu UV-3600 Plus UV–vis–NIR spectrophotometer equipped with an integrating sphere. With BaSO$_4$ as the standard reference, the detection range was set at 300 ∼ 1000 nm. The reflection measurement results were converted to the absorption spectra using the Kubelka–Mulk formula, and the band gap value E$_g$ was calculated according to the Tauc plot.

Photoluminescence (PL) spectra were acquired on a Hitachi F-4600 fluorescence spectrophotometer. The excitation wavelength was 325 nm, and the detection range of fluorescence emission was 340 ∼ 580 nm.

2.4. Photocatalytic glycerol oxidation and product analysis

Aqueous-phase aerobic glycerol oxidation reaction was conducted in a 20 mL glass reactor under ambient air conditions at room temperature. In a typical run, 64 mg AuPt/TiO$_2$ was well dispersed into 12 mL aqueous solution containing 66.67 mM glycerol and 0.15 M Na$_2$B$_4$O$_7$, and the initial pH value was measured as 9.2. A full-spectrum Perfect-Light PLS-SXE300 xenon lamp, equipped with an AM 1.5 G filter, was applied as the simulated sunlight source (intensity ≈ 200 mW/cm^2). The reaction mixture was stirred constantly at 1000 rpm to facilitate the mass transfer. For reaction kinetics analysis, 0.5 mL aliquot was extracted at specific time intervals and centrifuged to remove any adsorbed catalyst prior to analysis. A procedure identical to that outlined above was followed for a simulated accelerating process by adding certain amount of FA at the beginning of the reaction.

The separated liquid-phase products were quantitatively analyzed by high-performance liquid chromatography (HPLC) using Thermo Scientific Ultimate 3000 equipment with a multi-wavelength diode array detector (DAD-3000RS). The compounds were separated on a Chrom-Core Sugar-10 H column (8 μm, 300 × 7.8 mm) at 65 °C. During the measurements, 5 mM H$_2$SO$_4$ was used as the mobile phase at a flow rate of 0.5 mL/min. Quantitative analysis of the reaction compounds was achieved through the external calibration method using standard samples, which were provided in our previous reports [23–25]. Additionally, glycerol conversion, product selectivity, and yield were determined based on the following equations:

$$conversion \ (\%) = \frac{moles \ of \ consumed \ glycerol}{moles \ of \ initial \ glycerol} \times 100 = \frac{\Delta n_{GLY}}{n_{GLY,0}} \times 100 \tag{1}$$

$$selectivity \ (\%) = \frac{moles \ of \ certain \ product}{moles \ of \ consumed \ glycerol} \times 100 = \frac{i \times moles \ of \ C_i \ product}{3 \times \Delta n_{GLY}} \times 100 \tag{2}$$

$$yield \ (mmol \bullet g^{-1}) = \frac{moles \ of \ certain \ product}{mass \ of \ catalyst} \tag{3}$$

2.5. Reactive oxygen species evaluation

Colorimetric methods were applied for the detection of ·OH, ·O$_2^-$ and H$_2$O$_2$ in 0.15 M borate buffer (∼pH 7) under different conditions, using a Shimadzu UV-3600 spectrophotometer. The de-colorization rate of MB can be used for qualitative evaluation of ·OH. 25 mM MB solution containing 1 g/L photocatalysts was stirred in the dark to disperse evenly and attain the adsorption equilibrium. After the solution mixture was subjected to light irradiation under aerobic conditions, 1 mL aliquot was extracted at specific time intervals and centrifuged to separate the solid catalyst prior to detection. After centrifugation, the supernatant was taken into a quartz cuvette and the absorbance at 665 nm was measured. Likewise, the bleaching kinetics of NBT (50 μM) can be followed by measuring its absorbance peak at 259 nm under the same photocatalytic conditions, which reflects the photogenerated ·O$_2^-$ levels in the solution. The degradation kinetics of MB and NBT were fitted by first-order reaction kinetics (Eq. 4) with apparent rate constant values k.

$$c = c_0 \bullet e^{-kt} \tag{4}$$

Qualitative evaluation of solution H$_2$O$_2$ level was achieved by a colorimetric method using TMB, an indicator commonly used in enzymatic catalysis reactions to visualize the presence of H$_2$O$_2$, where TMB could be oxidized by hydrogen peroxide, and the solution would turn blue with a characteristic absorption peak at 652 nm. More quantitative determination of H$_2$O$_2$ level was conducted using a cobalt−carbonate assay following the literature report,[49] where H$_2$O$_2$ oxidizes Co^{2+} in the presence of bicarbonate, which exists in the form of Co(CO$_3$)$_3^{3-}$ complex. Specifically, 250 μL 0.07 M CoSO$_4$ solution was mixed with 19.5 mL 2 M KHCO$_3$ in borate solution and stirred in the dark for more than 30 min. Then, 1 g/L catalyst was added to the pre-mixed complex solution, and placed under light irradiation. 200 μL aliquot was extracted at specific time intervals before centrifugation, and the supernatant was diluted 16 times to facilitate kinetic measurements. H$_2$O$_2$ concentrations were determined from the corresponding absorbance of the Co(CO$_3$)$_3^{3-}$ complex at 257 nm. Note that the control experiments with various scavengers were also conducted following the same way. The standard calibration curve in borate buffer was obtained by

colorimetric testing using H_2O_2 solution at a series of known concentrations. In principle, the formation and decomposition of H_2O_2 on the catalyst surface would follow the zero-order and first-order reaction kinetics, respectively, and the respective formation (k_f) and decomposition (k_d) rate constant can be obtained by fitting the data curve using the following equation:

$$c[H_2O_2] = \frac{k_f}{k_d}[1 - \exp(-k_d t)] \quad (5)$$
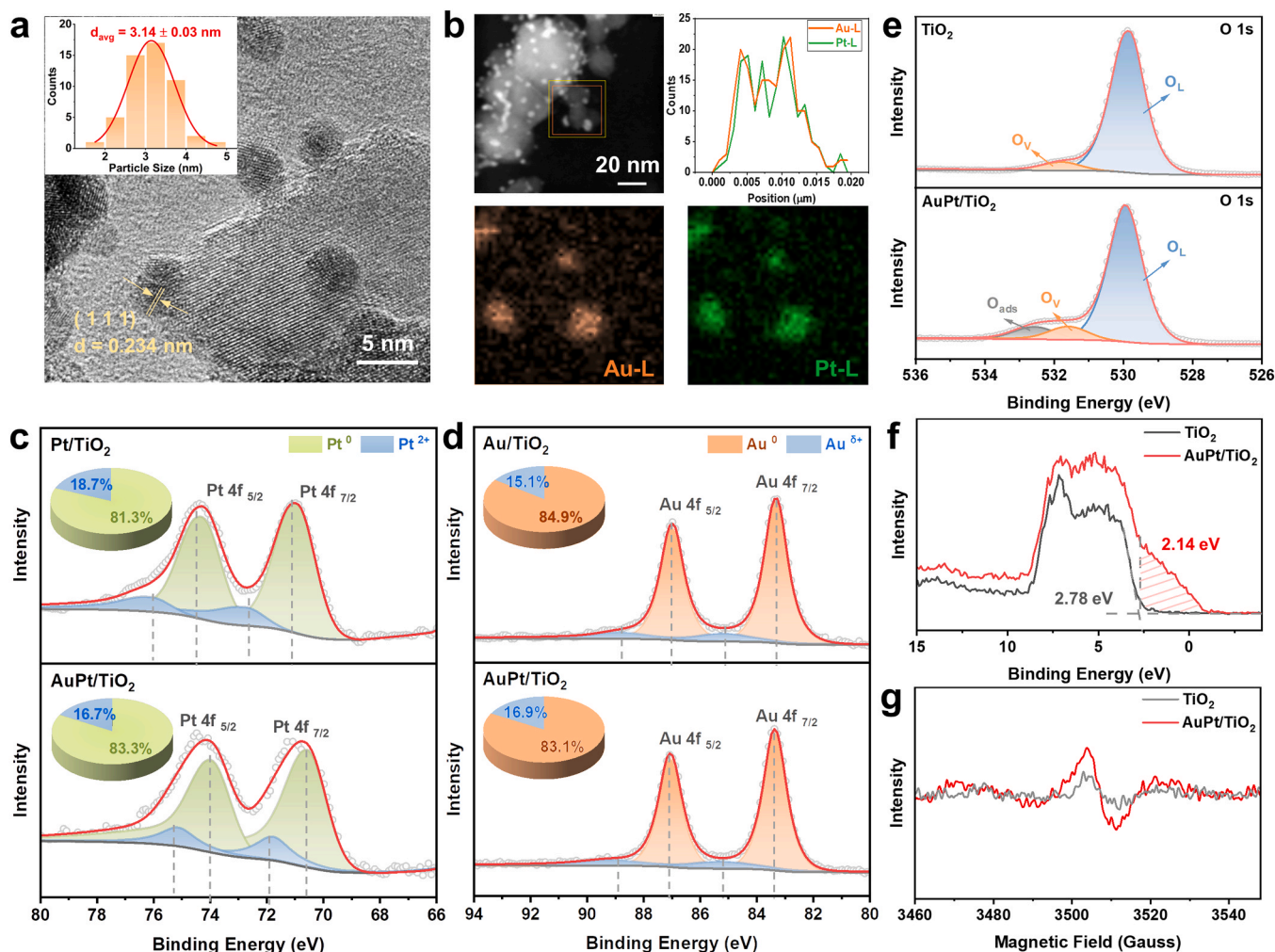
2.6. Quasi-in-situ Raman characterization

AuPt/TiO$_2$ was dispersed in 0.15 M borax solution and stirred for 1 h, to assure catalyst surface borate anions adsorption equilibrium was reached. After removing the majority of water by centrifugation, the thicker suspension was dropped onto a silicon wafer and dried at room temperature. This substrate was then placed into a 35 mm×10.5 mm culture dish, and 5 mL borate buffer solution was added to immerse the substrate with a liquid surface depth of ~5 mm. The Raman scattering spectra were recorded on a confocal Raman spectrometer (Renishaw InVia Qontor), using a 50 × Leica microscope objective with a numerical aperture of 0.50. When the field of view appeared legible, the power of the white light was kept being the largest, and the signals with certain time intervals were collected. The excitation wavelength was 532 nm,

and the Raman signals ranging from 268 cm^{-1} to 2005 cm^{-1} were collected, by recording and averaging three consecutive spectra with 1 s acquisition time per spectrum. During the data collection intervals, the samples were continuously exposed to the white light illumination from the mercury lamp. Baseline correction and peaks fitting with the Gaussian function of the Raman scattering spectra were performed using Origin 2023 software.

3. Result and discussion

3.1. Catalyst characterization

AuPt/TiO$_2$ catalysts were prepared by sol immobilization method with initial feeding molar ratio of Au:Pt at 1:1 (unless otherwise noted). The as formed AuPt (4 wt%) nanoparticles were homogeneously and discretely decorated on the Aeroxide TiO$_2$ (P25) supports, as shown by the low-resolution TEM image (Fig. S1). High-resolution TEM (HRTEM) image (Fig. 1a) revealed that the average diameter of AuPt on TiO$_2$ was about 3.14 nm with very narrow particle size distributions (Fig. 1a, inset), which was in good crystalline form displaying clear lattice fringes. Due to the relative small sizes and low loading amount of AuPt on TiO$_2$, no obvious diffraction peaks other than those of TiO$_2$ could be identified in the X-ray diffraction (XRD) patterns of AuPt/TiO$_2$ (Fig. S2). In order to unveil whether the AuPt nanoparticles existed in the form of

Fig. 1. (a) High-resolution TEM image, with the inset showing the histogram of the measured AuPt NPs diameters; (b) selected-area high-angle annular dark-field scanning transmission electron microscopy (HAADF-STEM) image, with the corresponding STEM-EDS line-scan and elemental mapping images; high-resolution X-ray photoelectron spectra (XPS) of (c) Pt 4 f and (d) Au 4 f. High-resolution O 1 s XPS spectra (e), valence-band XPS spectra (f), and EPR spectra (g) of TiO$_2$ and AuPt/TiO$_2$.

core-shell structures or alloys, selected-area high-angle annular dark-field scanning transmission electron microscopy (HAADF-STEM) imaging with energy-dispersive spectroscopy (EDS) was conducted. Both the corresponding color-coded elemental mapping images and the line-scan profiles reveal that the regions of Au and Pt overlapped perfectly, with nearly identical Au-L and Pt-L line-scan profiles (Fig. 1b), suggesting thus formed AuPt nanoparticles on TiO_2 were likely bimetallic AuPt alloys. Control samples of Au/TiO_2 and Pt/TiO_2 were prepared similarly, which also showed small discrete metal nanoparticles on TiO_2 supports (Fig. S3), with no apparent XRD peaks that can be identified to the metallic component either (Fig. S4).

The bimetallic alloy nature of AuPt nanoparticles supported on TiO_2 was further confirmed by X-ray photoelectron spectroscopy (XPS) analysis. As shown in Fig. 1c (lower panel), two pairs of peaks corresponding to Pt $4f_{7/2}$ and Pt $4f_{5/2}$ can be fitted in the high-resolution XPS spectrum of Pt 4f. The peaks with binding energy (BE) centered at 70.6 and 74.0 eV can be assigned to the Pt^0 metallic state, whereas the other peaks centered at 71.9 and 75.3 eV were in good agreement with oxidized Pt^{2+} species. Similarly, two pairs of peaks ascribed to Au $4f_{7/2}$ and Au $4f_{5/2}$ can be fitted in the high-resolution XPS spectrum of Au 4f (Fig. 1d, lower panel), with the peaks of binding energy centered at 83.4 and 85.3 eV corresponding to Au $4f_{7/2}$, and the peaks centered at 87.1 and 89.0 eV originating from Au $4f_{5/2}$. These fitted binding energies agreed well with Au^0 and $Au^{\delta+}$ chemical states. Compared with the monometallic samples (Au/TiO_2 and Pt/TiO_2), the BE of Pt 4f in $AuPt/TiO_2$ reduced by 0.6 eV, whereas the BE of Au 4 f shifted positively by 0.1 eV (Fig. 1c-d, upper panels), suggesting possible electron transfer from Au to Pt. By integrating the underlying XPS peak areas, the relative proportions of each species can be estimated. The percentage of Pt^0 species in $AuPt/TiO_2$ was determined to be 83.3%, which was 2.0% higher than that in Pt/TiO_2, with Pt^{2+} reduced correspondingly (Fig. 1c-d, insets). In addition, the proportion of Au^0 in $AuPt/TiO_2$ decreased by 1.8%, compared to that in Au/TiO_2, in line with the shift of binding energies of Pt 4 f and Au 4 f. The electron-rich Pt can facilitate electron transfer to oxygen in the oxygen reduction reactions, as demonstrated previously either by alloying [50] or metal-substrate interactions.[51]

Furthermore, the high-resolution XPS spectra of O 1 s (Fig. 1e) for $AuPt/TiO_2$ can be fitted by three peaks centered at 529.5, 531.5, and 532.5 eV, which are ascribed to the lattice oxygen (O_L), oxygen vacancy (O_v), and adsorbed oxygen (O_{ads}, surface hydroxyl and physically adsorbed oxygen species), respectively. It was observed that the ratio of oxygen vacancy to lattice oxygen (O_v/O_L) in pure TiO_2 was 0.144, while O_v/O_L increased slightly to 0.155 in $AuPt/TiO_2$. More striking difference lies in the appearance of the O_{ads} peak at 532.5 eV for $AuPt/TiO_2$ but not TiO_2, suggesting that AuPt can adsorb and activate O_2. The Ti 2p spectra (Fig. S5) of TiO_2 exhibited Ti^{4+} $2p_{3/2}$, Ti^{4+} $2p_{1/2}$, and the satellite peaks with BEs of 458.6, 464.3, and 471.8 eV, respectively. These BEs demonstrated subtle changes in the Ti 2p spectra of $AuPt/TiO_2$. In addition, the valence-band XPS (Fig. 1f) was used to identify the valence band maximum (VBM) of TiO_2 before and after loading the nanoalloy AuPt cocatalyst. It revealed that metal-induced occupied states (metallic d-orbital structure) were formed on the VBM of TiO_2 after the introduction of AuPt nanoalloy, which provided additional active sites and trapped the holes from the valence band of TiO_2 in photocatalysis, as reported previously [52]. The presence of O_V can also be investigated by conducting the room-temperature EPR spectra on TiO_2 and $AuPt/TiO_2$ (Fig. 1g), which showed g-factor values at 2.0038 correspond to O_V (g = 2.004). The EPR signal intensity of $AuPt/TiO_2$ was slightly stronger than that of TiO_2, consistent with the results shown in the XPS spectra of O 1 s.

The optical responses of the photocatalysts were evaluated by measuring their UV–vis–NIR diffuse reflectance spectra. As shown in Fig. S6a, Au/TiO_2 displayed a characteristic surface plasmon resonance (SPR) absorption peak centered at 560 nm, whereas a wide absorption band ($\lambda > 400$ nm) was observed for Pt/TiO_2 due to the intra-band and inter-band transitions of Pt [53]. While for $AuPt/TiO_2$, a broadened and

flattened absorption band appeared in the visible region, which could be attributed to the electronic interaction at the Au−Pt interface [54]. Based on their Tauc plots (Fig. S6b), the band gap energies of bare TiO_2, Au/TiO_2, Pt/TiO_2, and $AuPt/TiO_2$ were estimated to be 3.20, 3.30, 3.22, and 3.24 eV, respectively. The slightly widened band gaps indicated possible electron transfer from TiO_2 substrate to the metallic sites [55]. Steady-state photoluminescence (PL) spectra revealed that $AuPt/TiO_2$ displayed a weaker fluorescence peak at 380 nm, implying its better photo-generated e^-/h^+ pair separation efficiency (Fig. S6c).
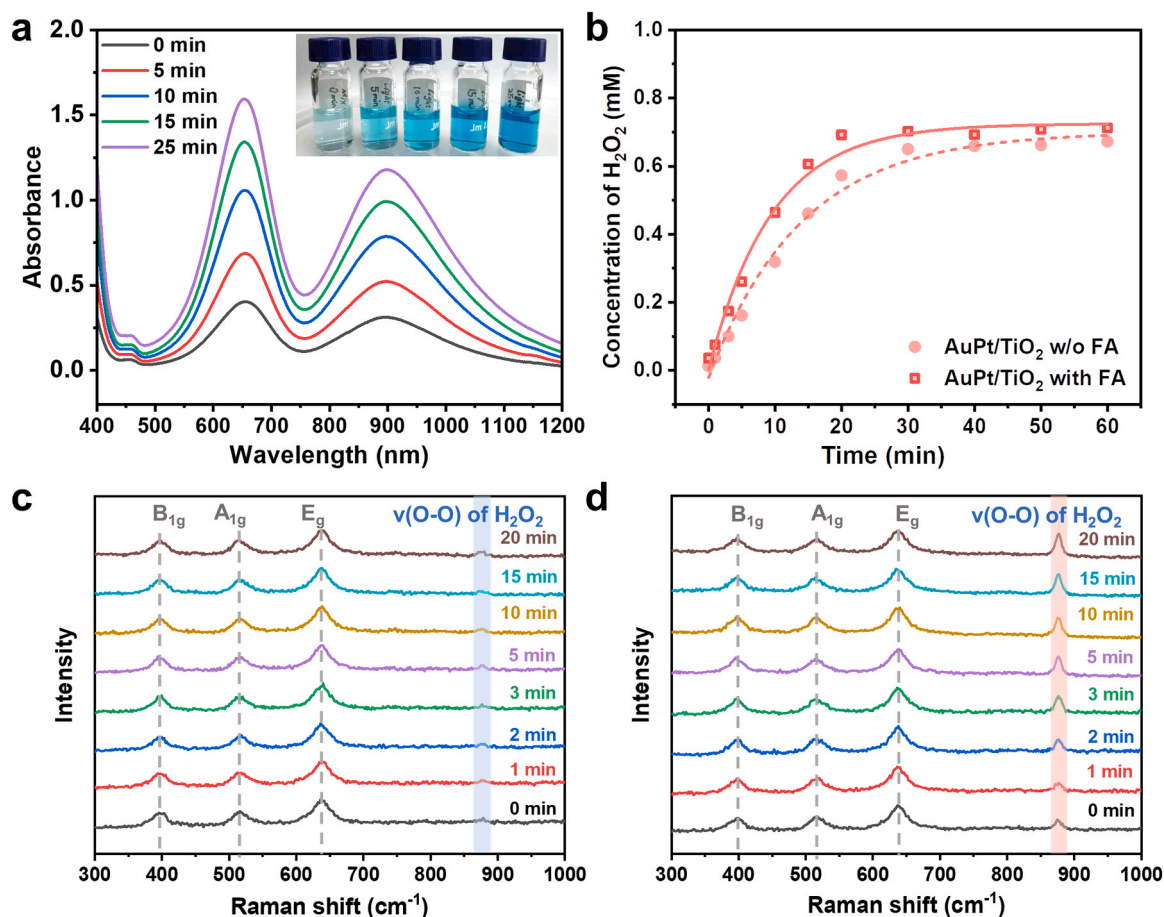
3.2. Photocatalytic H_2O_2 production and formate oxidase mimicking activity

Noble metal/TiO_2 catalysts have been demonstrated to produce H_2O_2 under light irradiation, which can be further enhanced in the presence of certain specific anions,[56] such as borate ions [57]. To illustrate the photocatalytic production of H_2O_2 on $AuPt/TiO_2$, TMB was first employed as a visual indicator for qualitative and semi-quantitative evaluation of the generated H_2O_2 levels. Under irradiation, the color of TMB solution containing $AuPt/TiO_2$ changed gradually to blue as a function of illumination time, with the absorbance at 652 nm intensified (Fig. 2a). Similar phenomena were observed for Au/TiO_2 (Fig. S7a) and Pt/TiO_2 (Fig. S7b). According to the solution optical absorbance at 652 nm, the level of photocatalytically produced solution H_2O_2 followed the order of $AuPt/TiO_2 \sim Pt/TiO_2 > Au/TiO_2$ (Fig. S8).

More quantitative results of solution H_2O_2 concentrations were obtained by a colorimetric method using cobalt-carbonate assays (detailed procedures in the Experimental Section), where the absorbance changes at 257 nm scaled linearly with H_2O_2 concentrations. By firstly obtaining the standard curves using known concentrations of H_2O_2 in both deionized water and borate buffer (Fig. S9), it was observed that the rate of H_2O_2 formation over $AuPt/TiO_2$ with borate was higher compared to that in the pure aqueous solution (Fig. S10), in good agreement with literature reports that borate anions can facilitate O_2 reduction to H_2O_2. [57,58]

Next, the photocatalytic formate oxidase (FOD) mimicking activity, which is the generation of H_2O_2 in the presence of formic acid, was evaluated by quantitative measurements using the cobalt-carbonate assays. The photocatalytic H_2O_2 formation (Fig. S11, Fig. 2b) was accelerated considerably when 0.6 mM FA was added into the $AuPt/TiO_2$ suspension (borate buffer, pH 7.0). By fitting the temporal evolution of solution H_2O_2 using Eq. 5, the formation (k_f) and decomposition (k_d) rate constant of H_2O_2 on $AuPt/TiO_2$ can be obtained. It was shown that k_f increased by ~30% in the presence of FA, whereas k_d remained nearly the same (Table S1). On the other hand, on both Pt/TiO_2 (Fig. S12) and Au/TiO_2 (Fig. S13), the temporal evolution curves of solution H_2O_2 varied little with and without formic acid addition (Fig. S14), indicating a lack of FOD activity on the similarly prepared monometallic noble metal nanoparticles supported on TiO_2. Moreover, as shown in Fig. S14, the initial H_2O_2 formation rate on Pt/TiO_2 was considerably faster than that on Au/TiO_2, but the final equilibrium solution H_2O_2 concentrations were comparable for the two photocatalysts (0.65 mM after 15 min of irradiation on Pt/TiO_2 vs. 0.7 mM after 1 h of irradiation on Au/TiO_2), likely due to slower decomposition rate of H_2O_2 on Au/TiO_2 than that on Pt/TiO_2, which is in good agreement with previous literature report.[37] The fitted rate constants of k_f and k_d for $AuPt/TiO_2$, Pt/TiO_2 and Au/TiO_2 were tabulated in Table S1, in borate buffer solution with and without formic acid addition.

Having established that H_2O_2 formation can be significantly accelerated on $AuPt/TiO_2$ in the presence of formic acid, we went further to characterize the surface peroxide species utilizing quasi-in-situ Raman scattering spectroscopy directly. As shown in Fig. 2c, three strong scattering peaks centered at 397, 515, and 637 cm^{-1} can be clearly identified, which are assigned to the B_{1g}, A_{1g}, and E_g modes of the anatase phase,[59] respectively. These peaks appeared almost unaffected under light illuminations. A rather weak scattering peak

Fig. 2. (a) UV–vis–NIR spectra of TMB in borate buffer solution containing AuPt/TiO$_2$ under light irradiation, with the inset photographs displaying the visual color changes of TMB solution as a function of illumination duration; (b) the temporal evolution of measured solution H$_2$O$_2$ concentrations in the absence (filled circles) and presence of FA (hollow squares), and the dashed and solid lines are the fitting curves based on Eq. 5; quasi-in-situ Raman spectra of surface H$_2$O$_2$ formation as a function of irradiation time in borate buffer without (c) and with (d) externally added FA.
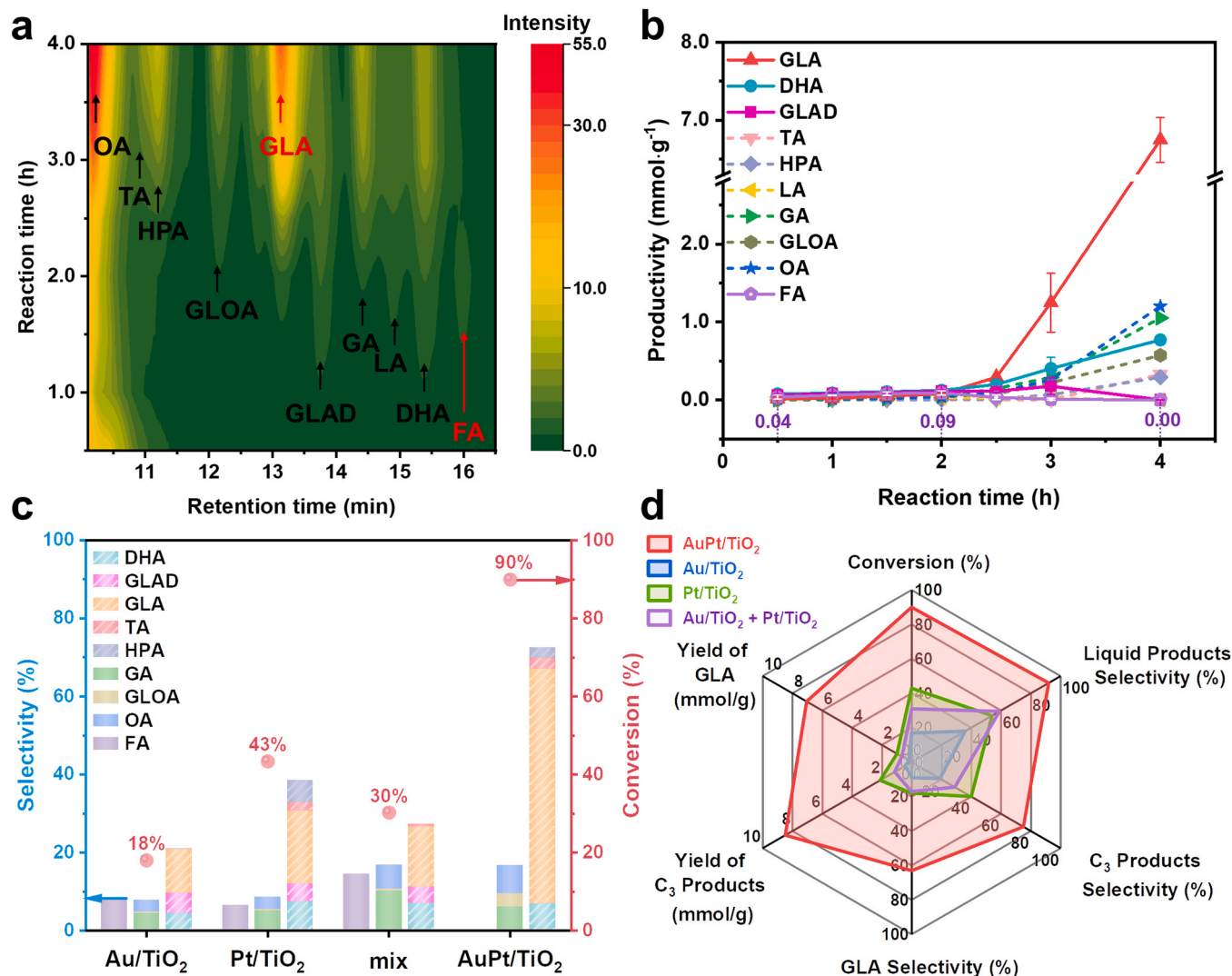
appearing at 876 cm^{-1} was attributed to the O-O vibration mode of H$_2$O$_2$ species [60,61], which displayed very subtle changes under illumination conditions. In stark contrast, upon adding formic acid into the solution, the Raman scattering peak at 876 cm^{-1} became stronger, and intensified upon extended light irradiation (Fig. 2d), demonstrating formic acid promoted surface peroxide formation on AuPt/TiO$_2$, especially under photo illumination. By normalizing the intensity of 876 cm^{-1} peak to that of the TiO$_2$ E$_g$ peak at 637 cm^{-1}, the temporal evolution of surface peroxide species as a function of illumination time can be obtained and compared (Fig. S15), demonstrating the critical role of formic acid played in promoting the photocatalytic H$_2$O$_2$ generation on AuPt/TiO$_2$.

3.3. Photocatalytic glycerol oxidation on FOD-mimicking AuPt/TiO$_2$

Given that the presence of formic acid can accelerate H$_2$O$_2$ formation on AuPt/TiO$_2$, we then went on to investigate this effect on the photocatalytic glycerol oxidation process. By deliberately adding formic acid into glycerol solution, the initial photocatalytic oxidation rate and products distribution were first analyzed and compared. The HPLC chromatogram of the solution products taken after 30 and 60 min of photocatalytic reaction were compiled in Fig. S16a. With the extra addition of FA (0.62 mM), it was noteworthy that the peak intensity of FA in HPLC chromatogram diminished completely in an hour, while that of GLA, DHA, and GA grew substantially over time, showing much stronger peak intensities than those from glycerol oxidation reaction performed without the externally added FA. Quantitative analysis of

each oxidation products (except FA) revealed significantly more pronounced GLA production, in the presence of added FA (Fig. S16b). After 1 h of photocatalytic reaction with FA addition, 0.36 mmol g$_{cat}^{-1}$ GLA, 0.22 mmol g$_{cat}^{-1}$ DHA, and 0.23 mmol g$_{cat}^{-1}$ C2 products (including GA, GLOA, and OA) were produced. The yield of GLA was increased by nearly 20.6 times compared to that of the inherent yield without FA addition. The above results showed that in the presence of FA, the photocatalytic glycerol oxidation kinetics on AuPt/TiO$_2$ was greatly accelerated, with altered oxidation product distributions, where production of GLA was enhanced considerably.

Noticing that FA itself is the glycerol oxidation product (Fig. S16a), which is known from our own as well as reported results from other research labs, we wonder whether the in situ generated formate species can be utilized for enhancing the actual photocatalytic glycerol oxidation process, without externally supplemented FA. Therefore, aerobic photocatalytic oxidation of glycerol on AuPt/TiO$_2$ in borate buffer solution (pH 9) was conducted under AM 1.5 G light irradiation, with the oxidation products analyzed over the reaction course of 4 h. By examining the temporal evolution of the HPLC chromatogram (Fig. 3a) and the quantitative productivity of the various glycerol oxidation products (Fig. 3b), we noticed that the FA productivity reached its maximum (0.09 mmol·g$_{cat}^{-1}$) after 2 h of photocatalytic reaction, and then started to decline. Meanwhile, GLAD and DHA were produced and accumulated progressively over this period, which also underwent further oxidation to generate products such as GLA, GA, and OA. A critical point was observed between 2.5 and 3 h of reaction time, when a sudden surge of GLA production was observed, accompanied by slightly delayed

Fig. 3. (a) 2D HPLC contour plot of the temporal liquid-phase oxidation products from the photocatalytic glycerol oxidation on AuPt/TiO$_2$ in borate buffer solution (pH 9); (b) calculated productivities of the various detected oxidation products as a function of reaction time (averaged over 3 parallel experiments); (c) the respective glycerol conversion, products selectivity, and (d) the comparison of the radar chart on Au/TiO$_2$, Pt/TiO$_2$, their physical mixture, and the alloy AuPt/TiO$_2$ samples, after 4 h of photocatalytic reaction in borate buffer solution.

descending GLAD levels. To the best of our knowledge, this induction and self-accelerating phenomenon in glycerol oxidation reaction has not been reported before. In terms of product selectivity, the selectivity toward C3 products decreased continuously during the first two hours, likely due to their further oxidation through C-C bond breakage, producing various C2 products and FA. On the other hand, the selectivity toward FA gradually increased to 2.3% after 1 h of reaction, then started to decline and dropped to background level as of 2.5 h (Fig. S17). As for the glycerol conversion rate, a steady increase was seen with prolonged reaction duration, until reaching the critical point of 2.5–3 h, after which the glycerol conversion surged from 38% to 90% in 1 h (Fig. S18). The coincidence of the FA depletion and the surging GLA production, indicate the in situ generated FA may be converted to H$_2$O$_2$ due to the FOD-mimicking activity of AuPt/TiO$_2$, which then accelerated the oxidation of glycerol toward GLA. After 4 h of photocatalytic reaction, 6.75 mmol·g$_{cat}^{-1}$ of GLA was produced at 90% glycerol conversion, with a high selectivity of 60%.

To further illustrate the unique glycerol oxidation behavior on the FOD-mimicking AuPt/TiO$_2$ photocatalysts, comparative investigations were also conducted on the aerobic glycerol oxidation using Au/TiO$_2$, Pt/TiO$_2$, as well as physically mixed Au/TiO$_2$ and Pt/TiO$_2$ as

photocatalysts under AM 1.5 G light irradiation for 4 h in borate buffer at pH 9 (Fig. 3c). Photocatalytic glycerol oxidation on Au/TiO$_2$ yielded DHA, GLAD, GLA, GA, OA, and FA in the liquid phase, with a 21% C3 products selectivity and 8% FA at 18% conversion. Apart from a higher glycerol conversion (43%) on Pt/TiO$_2$, an evident increase in the C3 products selectivity was also observed, reaching a 39% selectivity for DHA, GLAD, GLA, tartronic acid (TA), and hydroxypyruvic acid (HPA) combined, while the selectivity towards FA decreased to 6%. The physical mixture of Au/TiO$_2$ and Pt/TiO$_2$ with equal mass displayed moderate activity (30% conversion) and selectivity (27% C3 products), lying between that of the individual photocatalyst. The most pronounced difference in the product distribution was the lack of FA, when AuPt/TiO$_2$ was used as the photocatalyst, in line with the results that only AuPt/TiO$_2$ displayed FOD-mimicking activity. The numerical values of yields toward specific products and conversion are tabulated in Table S2, with the calculated carbon balances. The carbon balance remained ~90% for AuPt/TiO$_2$ after 4 h of reaction. The radar chart shown in Fig. 3d display more clearly the superb glycerol oxidation performance from alloy AuPt compared to its individual components. Furthermore, AuPt alloys with different molar ratios of Au and Pt loaded on TiO$_2$ were also tested for photocatalytic glycerol oxidation under the
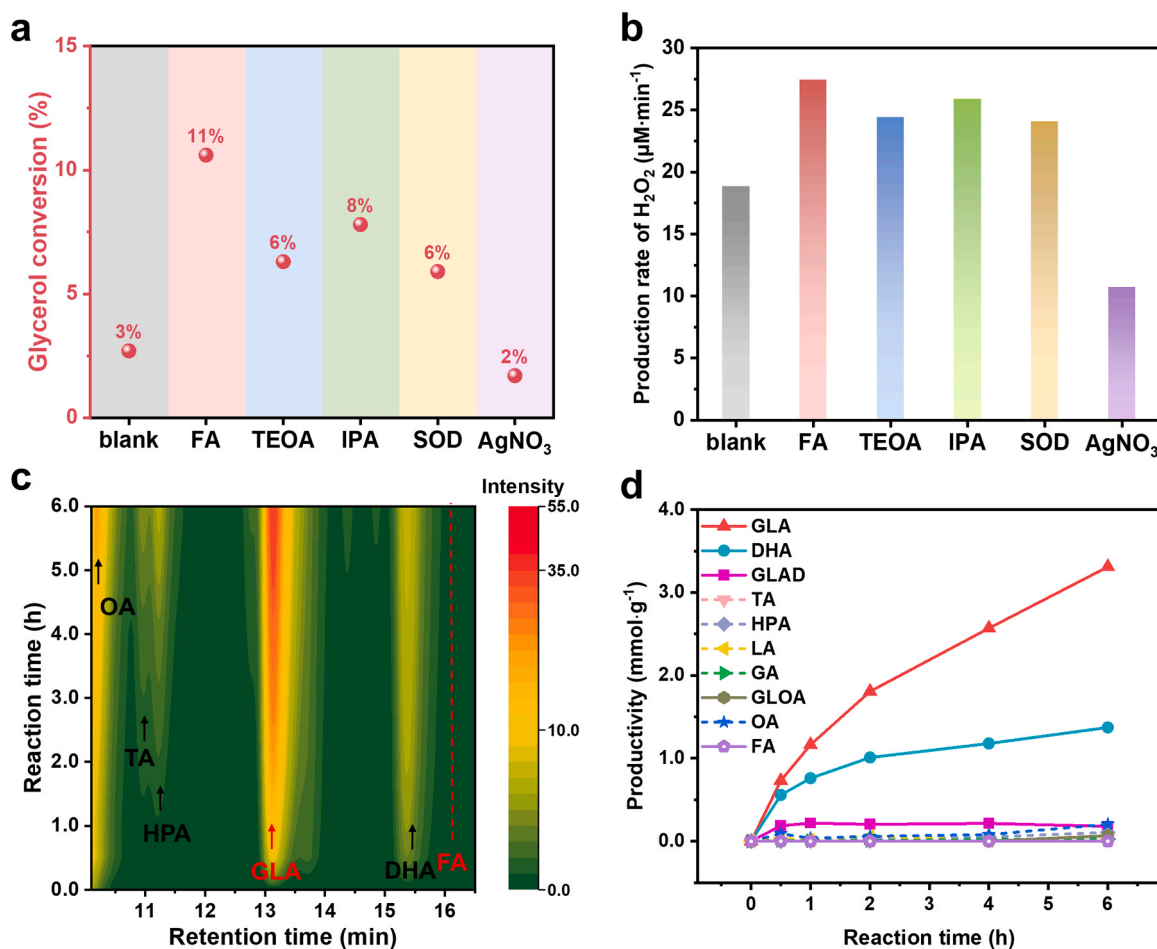
same experimental conditions (pH 9 borate buffer, 4 h photo illumination). As shown in Fig. S19, the glycerol conversion on Au_2Pt_1/TiO_2 decreased to 40% with a 63% C3 products selectivity. While on Au_1Pt_2/TiO_2, a faster reaction rate (64% conversion) was achieved, at the expense of lower C3 products selectivity (44%). Under current experimental conditions, $AuPt/TiO_2$ photocatalysts with equal molar amount of Au and Pt demonstrated the best glycerol oxidation performance, both in terms of activity (90% conversion) and C3 products selectivity (72%). Moreover, the contribution of surface plasmon resonances toward the observed photocatalytic glycerol oxidation can be largely ruled out, as the glycerol conversion on Au/TiO_2 (which displays the most pronounced surface plasmon resonances) was significantly lower (~6% after 4 h of reaction), despite using a 532 nm laser with much higher intensity (1.5 W cm^{-2}) as the excitation light source (Fig. S20). While in the absence of loaded noble metal catalysts, TiO_2 alone displayed moderate activity, with FA as the major solution products, as reported in our previous work [25]. The above results suggest that photo-excited charge carriers are mainly formed in TiO_2, whereas the loaded noble metal catalysts exert great influence on the solution ROS and glycerol oxidation selectivity. The demonstrated superb GLA selectivity at near complete glycerol conversion under ambient air at room temperature using $AuPt/TiO_2$ as photocatalyst, outperforms many of the recently published research works using TiO_2 based photocatalysts (Table S3).

Considering that photon absorption may vary for different catalysts given the changes in their respective optical spectra (Fig. S6a), by adopting the six-flux model, [62–64] the specific scattering (σ^*) and absorption (κ^*) coefficients for the used catalysts in a simplified reactor model (Table S4) were calculated (detailed description in the Supporting Information) and tabulated in Table S5. The apparent optical thickness (τ_{app}) as a function of catalyst concentrations were then obtained and tabulated in Table S6, together with the local volumetric rate of photon absorption (LVRPA) as a function of catalyst concentration calculated and plotted in Fig. S21. The optical thickness and photon absorption rates of $AuPt/TiO_2$ and Au/TiO_2 are approximately the same at equal concentrations, and the light absorption efficiency of Pt/TiO_2 is slightly lower than that of the former two, indicating that the dramatically improved catalytic activity of $AuPt/TiO_2$ is intrinsic.

3.4. Mechanistic study of selective partial glycerol oxidation on $AuPt/TiO_2$

The observed unprecedented induction and self-accelerating behaviors in the glycerol oxidation reaction on $AuPt/TiO_2$ is well correlated with its FOD-mimicking activity, where FA was consumed and O_2 was reduced to H_2O_2. Apart from H_2O_2, several other species, including photogenerated electrons (e^-) and holes (h^+), hydroxyl radicals ($\cdot OH$), as well as superoxide ($\cdot O_2^-$), could also play some direct and indirect roles in the glycerol oxidation processes. To identify their specific contributions, we employed different sacrificial agents, $AgNO_3$, triethanolamine (TEOA), isopropyl alcohol (IPA), and superoxide dismutase (SOD), to capture e^-, h^+, $\cdot OH$, and $\cdot O_2^-$, respectively. Interestingly, as shown in Fig. 4a, all of the scavengers used (except $AgNO_3$) expedited glycerol oxidation rate, in good correlation with the corresponding measured solution H_2O_2 levels (Fig. 4b), suggesting O_2 reduced by photogenerated

Fig. 4. Effect of different scavengers on the photocatalytic (a) glycerol oxidation rate and (b) H_2O_2 production rate, with the blank and FA serving as the negative and positive controls, respectively; (c) 2D HPLC contour plot and (d) calculated average productivity (n=3) of the various liquid-phase glycerol oxidation products on $AuPt/TiO_2$ in borate buffer solution (pH 9) with H_2O_2 as the oxidant, as a function of reaction time (reaction conducted in the dark).

electrons played the most critical role in the glycerol oxidation reaction on AuPt/TiO$_2$. Compared to that without any scavengers added, the increased production of H$_2$O$_2$ by adding TEOA and IPA is likely due to the improved photogenerated e$^-$/h$^+$ separation. Meanwhile, the improved H$_2$O$_2$ generation upon SOD addition rules out the disproportion or further reduction of ·O$_2^-$ as the major pathway for H$_2$O$_2$ formation, highlighting the existence of direct 2e$^-$ O$_2$ reduction pathway to H$_2$O$_2$ on AuPt/TiO$_2$.

Since the photocatalytic generation of H$_2$O$_2$ is positively correlated with the glycerol oxidation activity, as illustrated by the above results, we then carried out glycerol oxidation reaction at room temperature using externally added H$_2$O$_2$ as the only oxidant, while keeping the reaction away from light to avoid interference from other photogenerated reactive species. Upon gradual injection of 0.7 mM H$_2$O$_2$ into the reaction solution, the products elution peaks corresponding to GLA and DHA in the HPLC chromatogram appeared and intensified continually (Fig. 4c). Quantitatively speaking, the productivity of GLA and DHA reached a value of 3.31 and 1.37 mmol·g$_{cat}^{-1}$ after 6 h of reaction,

respectively (Fig. 4d). A steady increase in glycerol conversion was observed as a function of reaction time, increased from 25% after 0.5 h of reaction, to 65% after 6 h (Fig. S22a). However, the selectivity of GLA stayed nearly the same after 4 h at around 41%, and the C3 products selectivity remained constant at ~62% (Fig. S22b). Upon heating the reaction mixture to 60 °C, glycerol can be quickly oxidized by H$_2$O$_2$ in half an hour, achieving 82% glycerol conversion with a 46% GLA selectivity, and reaching complete conversion within 2 h, but with a reduced GLA selectivity at 28% (Fig. S23a-b). After glycerol was completely consumed, C3 products were then oxidized, resulting in further reduction of both GLA and total C3 products selectivity (Fig. S23b-c). The selectivity of C3 products dropped from 62% at the initial 0.5 h to 12% after 6 h, accompanied by increasing C2 products selectivity from 6% to 50%. GLA and DHA rapidly reached maximum yield (4.75 and 0.61 mmol·g$_{cat}^{-1}$), which were further oxidized to HPA, reaching its peak productivity at 1.27 mmol·g$_{cat}^{-1}$ after 2 h (Fig. S23d). Significant amount of C2 product OA was detected, increasing over time and reaching the maximum productivity of 8.93 mmol·g$_{cat}^{-1}$ after 6 h. We

Scheme 2. Illustration of the proposed (a) glycerol oxidation pathway, and (b) reaction mechanism of formic acid-promoted on-site H$_2$O$_2$ production over FOD-mimicking AuPt/TiO$_2$ for the selective photocatalytic glycerol upgrading.

postulated that the elevated temperatures not only enhanced glycerol oxidation kinetics, but also accelerated the decomposition of H_2O_2, generating reactive oxygen species which facilitated C-C bond cleavage to produce C2 products. Interestingly, there was also very little FA accumulation throughout the whole reaction period, due to the FOD-mimicking activity of AuPt/TiO₂. More surprising results came from glycerol oxidation reaction conducted in the dark using AuPt/TiO₂ as catalyst, 28% glycerol was converted after 4 h of reaction, with over 70% C3 products (DHA, GLAD, and GLA) selectivity (Fig. S24). We suspect this is due to the combined effect of initial low level of surface peroxide species formation on AuPt (as shown in Fig. 2) and its FOD activity. This is in stark contrast to glycerol oxidation on Au/TiO₂ reported by us previously,[25] where no oxidation products can be detected when the reaction was conducted in the absence of light illumination.

Based on the detected liquid phase oxidation products and their temporal evolution profiles, a tentative glycerol oxidation pathway is proposed, as illustrated in Scheme 2a. The oxidation of the terminal hydroxyl group is favored over the middle hydroxyl group on AuPt/TiO₂ by H_2O_2, producing mainly GLA instead of DHA, and further oxidation of GLA and DHA leads to the formation of TA and HPA, or to GA and FA by C−C bond breakage. GA was eventually oxidized to OA, while FA was oxidized and facilitated H_2O_2 generation.

The above results demonstrated that H_2O_2 can act as a mild oxidant to produce GLA and other C3 products from glycerol using AuPt/TiO₂ as catalyst. However, it cannot reach the same level of high GLA selectivity at relative high glycerol conversion under photocatalytic conditions. We postulate that the in situ generated H_2O_2 may react with the surface adsorbed glycerol located at nearby catalytic sites more easily, than the freely diffusing solution H_2O_2. Furthermore, FA consumed the photogenerated h^+, and facilitated the utilization of photogenerated e^- for direct O_2 reduction to H_2O_2. This is confirmed by measuring the photogenerated active species on AuPt/TiO₂ photocatalyst, with and without intentionally added FA. As expected, ROS such as $\cdot O_2^-$ and $\cdot OH$ were both reduced in the presence of FA (Fig. S25), with the generation rates dropped down by 2.1 and 2.4-fold, respectively (Table S7), which would be beneficial for high C3 products selectivity. However, due to the co-existence of various ROS and the complicated inter-conversion/reaction between them in solution,[17] it is difficult to delineate the exact role of each specific ROS, and only qualitative conclusions can be drawn from comparative studies by us [25] as well as by others [22], that $\cdot OH$ is highly oxidative and often driving complete substrate mineralization, while $\cdot O_2^-$ and H_2O_2 are much milder oxidant for value-added C3 products generation.

Based on the above evidence, a tentative mechanism of photocatalytic glycerol oxidation reaction self-expedited by on-site H_2O_2 production is proposed (Scheme 2b), where oxygen and glycerol oxidation product formic acid were utilized as the feedstock for H_2O_2 synthesis on FOD-mimicking AuPt/TiO₂ catalyst. Upon TiO₂ photo excitation by sunlight irradiation, electrons excited from the valence band to the conduction band were transferred to the AuPt alloy nanoparticles, which then reduced O_2 to form $\cdot O_2^-$ and H_2O_2; while the holes in the valence band can oxidize either glycerol directly or water to produce $\cdot OH$, which is a strong oxidant to oxidize glycerol to various products including FA. Upon FA generation, it competes with the $1e^-$ O_2 reduction, h^+ mediated water and direct glycerol oxidation processes, by consuming h^+ and promoting $2e^-$ O_2 reduction to H_2O_2. After gradual surface peroxide species accumulation at the active sites on AuPt as the result of continuous aerobic FA oxidation, a critical point is reached when glycerol is quickly oxidized by H_2O_2 to valuable C3 products (72% selectivity) dominated by GLA (60%) at high conversion (90%). Inevitably, GLA may undergo further oxidation to produce HPA, TA, as well as GA and OA by breaking a C-C bond.

This study opens up a new door for selective partial oxidation of glycerol utilizing its most commonly observed C1 product formic acid. The in situ generated FA not only suppress the direct and indirect deep oxidation of glycerol mediated by photogenerated holes, but also promote on-site H_2O_2 production to facilitate mild glycerol oxidation to valuable C3 products. We envision that by optimizing the metal catalyst as well as the semiconductor support, FOD-mimicking activity and the ultimate glycerol oxidation selectivity can be improved further. The insight into the selective glycerol oxidation reaction on FOD-mimicking catalyst may also be extended to other biomass oxidation reactions, in which formic acid is also a common oxidation product. Finally, a more detailed investigation on the catalyst surface-adsorbate interactions is required in future studies, in order to fully grasp the microscopic picture at the point when the critical turning point of the reaction kinetics is reached, which could also guide future catalyst design where surface functional groups and active site property may be exploited to modulate reaction selectivity.

4. Conclusion

Selective aerobic photocatalytic glycerol partial oxidation on AuPt/TiO₂ towards value-added C3 products has been achieved in borate buffer solution under ambient air at room temperature, with a unique self-accelerating reaction kinetics reported for the first time. Bimetallic AuPt/TiO₂ exhibits evident formate oxidase mimicking activity, with H_2O_2 production (0.71 $mmol \cdot g_{cat}^{-1} \cdot h^{-1}$) increased by over 30% in the presence of externally added formic acid under light irradiation, whereas monometallic Au/TiO₂ and Pt/TiO₂ do not show the same characteristics. By performing photocatalytic glycerol oxidation reaction with intentionally added formic acid, various e^-/h^+ and ROS scavengers, we find that the glycerol oxidation rate is positively correlated with the solution H_2O_2 level, which is a mild oxidant that oxidizes glycerol to mainly glyceric acid in the dark. Moreover, as formic acid is commonly formed in the process of glycerol oxidation, we discover that the photocatalytic glycerol oxidation on AuPt/TiO₂ experiences an induction period during which formic acid gradually accumulates to a maximum of 0.09 $mmol \cdot g_{cat}^{-1}$ after 2 h, then declines accompanied by a surging glyceric acid production. In weakly basic pH 9 borate buffer solution, a selectivity of 72% toward C3 chemicals (60% for glyceric acid) can be achieved at 90% glycerol conversion. Our findings presented herein may provide guidance for future catalyst design, where photocatalytic biomass valorization could be facilitated via on-site generation of H_2O_2.

CRediT authorship contribution statement

Yu Zou: Project administration, Supervision, Formal analysis, Methodology. **Xiaoyuan Liu:** Data curation, Investigation, Methodology, Writing – original draft. **Jiang Jiang:** Conceptualization, Formal analysis, Funding acquisition, Project administration, Writing – review & editing.

Declaration of Competing Interest

The authors declare that they have no known competing financial interests or personal relationships that could have appeared to influence the work reported in this paper.

Data Availability

Data will be made available on request.

Acknowledgments

Appendix A. Supporting information

Supplementary data associated with this article can be found in the online version at doi:10.1016/j.apcatb.2024.123927.

References

[1] M.R. Monteiro, C.L. Kugelmeier, R.S. Pinheiro, M.O. Batalha, A. da Silva César, Glycerol from biodiesel production: Technological paths for sustainability, Renew. Sustain. Energy Rev. 88 (2018) 109–122.

[2] M. Pagliaro, R. Ciriminna, H. Kimura, M. Rossi, C. Della Pina, From Glycerol to Value-Added Products, Angew. Chem., Int. Ed. 46 (2007) 4434–4440.

[3] C.-H. Zhou, J.N. Beltramini, Y.-X. Fan, G.Q. Lu, Chemoselective catalytic conversion of glycerol as a biorenewable source to valuable commodity chemicals, Chem. Soc. Rev. 37 (2008) 527–549.

[4] B. Katryniok, H. Kimura, E. Skrzyńska, J.-S. Girardon, P. Fongarland, M. Capron, R. Ducoulombier, N. Mimura, S. Paul, F. Dumeignil, Selective catalytic oxidation of glycerol: perspectives for high value chemicals, Green. Chem. 13 (2011) 1960–1979.

[5] G. Dodekatos, S. Schünemann, H. Tüysüz, Recent advances in thermo-, photo-, and electrocatalytic glycerol oxidation, ACS Catal. 8 (2018) 6301–6333.

[6] V. Maurino, A. Bedini, M. Minella, F. Rubertelli, E. Pelizzetti, C. Minero, Glycerol Transformation Through Photocatalysis: A Possible Route to Value Added, Chem., J. Adv. Oxid. Technol. 11 (2008) 184–192.

[7] V. Augugliaro, H.A.H. El Nazer, V. Loddo, A. Mele, G. Palmisano, L. Palmisano, S. Yurdakal, Partial photocatalytic oxidation of glycerol in TiO2 water suspensions, Catal. Today 151 (2010) 21–28.

[8] M.R. Karimi Estahbanati, M. Feilizadeh, F. Attar, M.C. Iliuta, Current developments and future trends in photocatalytic glycerol valorization: photocatalyst development, Ind. Eng. Chem. Res. 59 (2020) 22330–22352.

[9] M.R. Karimi Estahbanati, M. Feilizadeh, F. Attar, M.C. Iliuta, Current developments and future trends in photocatalytic glycerol valorization: process analysis, React. Chem. Eng. 6 (2021) 197–219.

[10] J. Payormhorm, R. Idem, Synthesis of C-doped TiO2 by sol-microwave method for photocatalytic conversion of glycerol to value-added chemicals under visible light, Appl. Catal., A 590 (2020) 117362.

[11] L. Xiong, H. Qi, S. Zhang, L. Zhang, X. Liu, A. Wang, J. Tang, Highly selective transformation of biomass derivatives to valuable chemicals by single-atom photocatalyst Ni/TiO2, Adv. Mater. 35 (2023) 2209646.

[12] G. Dodekatos, H. Tüysüz, Plasmonic Au/TiO2 nanostructures for glycerol oxidation, Catal. Sci. Technol. 6 (2016) 7307–7315.

[13] T. Jedsukontorn, N. Saito, M. Hunsom, Photocatalytic behavior of metal-decorated TiO2 and their catalytic activity for transformation of glycerol to value added compounds, Mol. Catal. 432 (2017) 160–171.

[14] T. Jedsukontorn, N. Saito, M. Hunsom, Photoinduced Glycerol Oxidation over Plasmonic Au and AuM (M = Pt, Pd and Bi) Nanoparticle-Decorated TiO(2) Photocatalysts, Nanomaterials 8 (2018) 269.

[15] L. Abis, N. Dimitritatos, M. Sankar, S.J. Freakley, G.J. Hutchings, Plasmonic oxidation of glycerol using AuPd/TiO2 catalysts, Catal. Sci. Technol. 9 (2019) 5686–5691.

[16] L. Abis, N. Dimitratos, M. Sankar, S.J. Freakley, G.J. Hutchings, Plasmonic Oxidation of Glycerol Using Au/TiO2 Catalysts Prepared by Sol-Immobilisation, Catal. Lett. 150 (2020) 49–55.

[17] Y. Nosaka, A.Y. Nosaka, Generation and detection of reactive oxygen species in photocatalysis, Chem. Rev. 117 (2017) 11302–11336.

[18] D. Yitao, Y. Xiong, Control of selectivity in organic synthesis via heterogeneous photocatalysis under visible light, Nano Res. Energy 1 (2022) 9120006.

[19] L. Xiong, J. Tang, Strategies and Challenges on Selectivity of Photocatalytic Oxidation of Organic Substances, Adv. Energy Mater. 11 (2021) 2003216.

[20] Z. Huang, N. Luo, C. Zhang, F. Wang, Radical generation and fate control for photocatalytic biomass conversion, Nat. Rev. Chem. 6 (2022) 197–214.

[21] P. Panagiotopoulou, E.E. Karamerou, D.I. Kondarides, Kinetics and mechanism of glycerol photo-oxidation and photo-reforming reactions in aqueous TiO2 and Pt/ TiO2 suspensions, Catal. Today 209 (2013) 91–98.

[22] M. Liu, H. Liu, N. Li, C. Zhang, J. Zhang, F. Wang, Selective oxidation of glycerol into formic acid by photogenerated holes and superoxide radicals, ChemSusChem 15 (2022) 202201068.

[23] X. Huang, Y. Zou, J. Jiang, Electrochemical Oxidation of Glycerol to Dihydroxyacetone in Borate Buffer: Enhancing Activity and Selectivity by Borate–Polyol Coordination Chemistry, ACS Sustain. Chem. Eng. 9 (2021) 14470–14479.

[24] X. Huang, Y. Guo, Y. Zou, J. Jiang, Electrochemical oxidation of glycerol to hydroxypyruvic acid on cobalt (oxy)hydroxide by high-valent cobalt redox centers, Appl. Catal., B 309 (2022) 121247.

[25] X. Liu, Y. Zou, J. Jiang, Selective aerobic photocatalytic glycerol oxidation on Au/ TiO2 with borate additives, Appl. Catal., A 660 (2023) 119216.

[26] D.I. Enache, J.K. Edwards, P. Landon, B. Solsona-Espriu, A.F. Carley, A.A. Herzing, M. Watanabe, C.J. Kiely, D.W. Knight, G.J. Hutchings, Solvent-free oxidation of primary alcohols to aldehydes using Au-Pd/TiO2 catalysts, Science 311 (2006) 362–365.

[27] B.N. Zope, D.D. Hibbitts, M. Neurock, R.J. Davis, Reactivity of the gold/water interface during selective oxidation catalysis, Science 330 (2010) 74–78.

[28] S.P. Teong, X. Li, Y. Zhang, Hydrogen peroxide as an oxidant in biomass-to-chemical processes of industrial interest, Green. Chem. 21 (2019) 5753–5780.

[29] Y. Kon, T. Nakashima, S.-y Onozawa, K. Sato, S. Kobayashi, , Switchable synthesis of aldehydes and carboxylic acids from alcohols by platinum-catalysed hydrogen peroxide oxidation using flow reactors, Adv. Synth. Catal. 364 (2022) 3372–3377.

[30] X. Wang, C. Shang, G. Wu, X. Liu, H. Liu, Base-Free Selective Oxidation of Glycerol over LDH Hosted Transition Metal Complexes Using 3% H2O2 as Oxidant, Catalysts 6 (2016) 101.

[31] M. Kapkowski, P. Bartczak, M. Korzec, R. Sitko, J. Szade, K. Balin, J. Lelątko, J. Polanski, SiO2-, Cu-, and Ni-supported Au nanoparticles for selective glycerol oxidation in the liquid phase, J. Catal. 319 (2014) 110–118.

[32] C.A. Nunes, M.C. Guerreiro, Chemometric approaches on glycerol oxidation with H2O2 over supported gold nanoparticles, J. Mol. Catal. A: Chem. 370 (2013) 145–151.

[33] M.L. Faroppa, J.J. Musci, M.E. Chiosso, C.G. Caggiano, H.P. Bideberripe, J.L. G. Fierro, G.J. Siri, M.L. Casella, Oxidation of glycerol with H2O2 on Pb-promoted Pd/Γ-Al2O3 catalysts, Chin. J. Catal. 37 (2016) 1982–1990.

[34] X. Wang, G. Wu, T. Jin, J. Xu, S. Song, Selective Oxidation of Glycerol Using 3% H2O2 Catalyzed by Supported Nano-Au Catalysts, Catalysts 8 (2018) 505.

[35] R. Underhill, M. Douthwaite, R.J. Lewis, P.J. Miedziak, R.D. Armstrong, D. J. Morgan, S.J. Freakley, T. Davies, A. Folli, D.M. Murphy, Q. He, O. Akdim, J. K. Edwards, G.J. Hutchings, Ambient base-free glycerol oxidation over bimetallic PdFe/SiO2 by in situ generated active oxygen species, Res. Chem. Intermed. 47 (2021) 303–324.

[36] M. Teranishi, S.-i Naya, H. Tada, In situ liquid phase synthesis of hydrogen peroxide from molecular oxygen using gold nanoparticle-loaded titanium(IV) dioxide photocatalyst, J. Am. Chem. Soc. 132 (2010) 7850–7851.

[37] H. Kobayashi, M. Teranishi, R. Negishi, S.-i Naya, H. Tada, Reaction Mechanism of the Multiple-Electron Oxygen Reduction Reaction on the Surfaces of Gold and Platinum Nanoparticles Loaded on Titanium(IV) Oxide, J. Phys. Chem. Lett. 7 (2016) 5002–5007.

[38] M. Teranishi, S.-i Naya, Y. Yan, T. Soejima, H. Kobayashi, H. Tada, A biomimetic all-inorganic photocatalyst for the artificial photosynthesis of hydrogen peroxide, Catal. Sci. Technol. 12 (2022) 6062–6068.

[39] H. Tada, M. Teranishi, S.-i. Naya, Hydrogen Peroxide Production by Inorganic Photocatalysts Consisting of Gold Nanoparticle and Metal Oxide toward Oxygen Cycle Chemistry, J. Phys. Chem. C. 127 (2023) 5199–5209.

[40] D. Tsukamoto, A. Shiro, Y. Shiraishi, Y. Sugano, S. Ichikawa, S. Tanaka, T. Hirai, Photocatalytic H2O2 Production from Ethanol/O2 System Using TiO2 Loaded with Au–Ag Bimetallic Alloy Nanoparticles, ACS Catal. 2 (2012) 599–603.

[41] M. Teranishi, R. Hoshino, S. Naya, H. Tada, Gold-nanoparticle-loaded carbonate-modified titanium(IV) oxide surface: visible-light-driven formation of hydrogen peroxide from oxygen, Angew. Chem., Int. Ed. 55 (2016) 12773–12777.

[42] Z. Chen, Y. Yu, Y. Gao, Z. Zhu, Rational Design Strategies for Nanozymes, ACS Nano 17 (2023) 13062–13080.

[43] M.S. Yalfani, S. Contreras, F. Medina, J. Sueiras, Direct generation of hydrogen peroxide from formic acid and O2 using heterogeneous Pd/gamma-Al2O3 catalysts, Chem. Commun. (2008) 3885–3887.

[44] L. Wang, M. Carta, R. Malpass-Evans, N.B. McKeown, P.J. Fletcher, P. Estrela, A. Roldan, F. Marken, Artificial formate oxidase reactivity with nano-palladium embedded in intrinsically microporous polyamine (Pd@PIM-EA-TB) driving the H2O2 – 3,5,3′,5′-tetramethylbenzidine (TMB) colour reaction, J. Catal. 416 (2022) 253–266.

[45] A. Mehri, H. Kochkar, In Situ Generated H2O2 over Supported Pd–Au Clusters in Hybrid Titania Nanocrystallites, Chem. Lett. 43 (2014) 1046–1048.

[46] J. Chen, Q. Ma, Z. Yu, M. Li, S. Dong, Platinum-Gold Alloy Catalyzes the Aerobic Oxidation of Formic Acid for Hydrogen Peroxide Synthesis, Angew. Chem., Int. Ed. 61 (2022) 202213930.

[47] G.L. Brett, Q. He, C. Hammond, P.J. Miedziak, N. Dimitratos, M. Sankar, A. A. Herzing, M. Conte, J.A. Lopez-Sanchez, C.J. Kiely, D.W. Knight, S.H. Taylor, G. J. Hutchings, Selective oxidation of glycerol by highly active bimetallic catalysts at ambient temperature under base-free conditions, Angew. Chem., Int. Ed. 50 (2011) 10136–10139.

[48] C.B. Paris, A.G. Howe, R.J. Lewis, D. Hewes, D.J. Morgan, Q. He, J.K. Edwards, Impact of the Experimental Parameters on Catalytic Activity When Preparing Polymer Protected Bimetallic Nanoparticle Catalysts on Activated Carbon, ACS Catal. 12 (2022) 4440–4454.

[49] T.M. Gill, X. Zheng, Comparing methods for quantifying electrochemically accumulated H2O2, Chem. Mater. 32 (2020) 6285–6294.

[50] W. Yan, D. Zhang, Q. Zhang, Y. Sun, S. Zhang, F. Du, X. Jin, Synthesis of PtCu–based nanocatalysts: Fundamentals and emerging challenges in energy conversion, J. Energy Chem. 64 (2022) 583–606.

[51] G. Chao, X. An, L. Zhang, J. Tian, W. Fan, T. Liu, Electron-rich platinum electrocatalysts supported onto tin oxides for efficient oxygen reduction, Compos. Commun. 24 (2021) 100603.

[52] C. Jin, Y. Dai, W. Wei, X. Ma, M. Li, B. Huang, Effects of single metal atom (Pt, Pd, Rh and Ru) adsorption on the photocatalytic properties of anatase TiO2, Appl. Surf. Sci. 426 (2017) 639–646.

[53] Y. Shiraishi, D. Tsukamoto, Y. Sugano, A. Shiro, S. Ichikawa, S. Tanaka, T. Hirai, Platinum nanoparticles supported on anatase titanium dioxide as highly active catalysts for aerobic oxidation under visible light irradiation, ACS Catal. 2 (2012) 1984–1992.

[54] L.M. Liz-Marzan, A.P. Philipse, Stable hydrosols of metallic and bimetallic nanoparticles immobilized on imogolite fibers, J. Phys. Chem. 99 (1995) 15120–15128.

[55] F. Zuo, K. Bozhilov, R.J. Dillon, L. Wang, P. Smith, X. Zhao, C. Bardeen, P. Feng, Active Facets on Titanium(III)-Doped TiO2: an effective strategy to improve the visible-light photocatalytic activity, Angew. Chem., Int. Ed. 51 (2012) 6223–6226.

[56] Y. Wang, Y. Wang, J. Zhao, Y. Xu, Effect of inorganic ions on H2O2 production over illuminated Au/WO3 with visible light, Appl. Catal., B 299 (2021) 120676.

[57] X. Xiong, X. Zhang, S. Liu, J. Zhao, Y. Xu, Sustained production of H2O2 in alkaline water solution using borate and phosphate-modified Au/TiO2 photocatalysts, Photochem. Photobiol. Sci. 17 (2018) 1018–1022.

[58] X. Xiong, Y. Xu, Synergetic effect of Pt and borate on the TiO2-photocatalyzed degradation of phenol in water, J. Phys. Chem. C. 120 (2016) 3906–3912.

[59] Y. Jiang, W. Zhao, S. Li, S. Wang, Y. Fan, F. Wang, X. Qiu, Y. Zhu, Y. Zhang, C. Long, Z. Tang, Elevating photooxidation of methane to formaldehyde via TiO2 crystal phase engineering, J. Am. Chem. Soc. 144 (2022) 15977–15987.

[60] S. Ahmad, J.D. McCallum, A.K. Shiemke, E.H. Appelman, T.M. Loehr, J. Sanders-Loehr, Raman spectroscopic evidence for side-on binding of peroxide ion to (ethylenediaminetetraacetato)ferrate(1-), Inorg. Chem. 27 (1988) 2230–2233.

[61] A.J. Simaan, S. Döpner, F. Banse, S. Bourcier, G. Bouchoux, A. Boussac, P. Hildebrandt, J.-J. Girerd, FeIII-Hydroperoxo and Peroxo Complexes with Aminopyridyl Ligands and the Resonance Raman Spectroscopic Identification of the Fe−O and O−O Stretching Modes, Eur. J. Inorg. Chem. 2000 (2000) 1627–1633.

[62] I. Grčić, G. Li, Puma, Six-flux absorption-scattering models for photocatalysis under wide-spectrum irradiation sources in annular and flat reactors using catalysts with different optical properties, Appl. Catal., B 211 (2017) 222–234.

[63] R. Acosta-Herazo, M.Á. Mueses, G.L. Puma, F. Machuca-Martínez, Impact of photocatalyst optical properties on the efficiency of solar photocatalytic reactors rationalized by the concepts of initial rate of photon absorption (IRPA) dimensionless boundary layer of photon absorption and apparent optical thickness, Chem. Eng. J. 356 (2019) 839–849.

[64] L. Hurtado, R. Natividad, E. Torres-García, J. Farias, G. Li, Puma, Correlating the photocatalytic activity and the optical properties of LiVMoO6 photocatalyst under the UV and the visible region of the solar radiation spectrum, Chem. Eng. J. 262 (2015) 1284–1291.